# Built-In Self Test of MEMS Accelerometers*

*N. Deb* and *R. D. (Shawn) Blanton*

Department of Electrical and Computer Engineering

Carnegie Mellon University, Pittsburgh, PA 15213

email: {ndeb, blanton}@ece.cmu.edu

## Abstract

*A built-in self-test technique that is applicable to symmetric microsystems is described. A combination of existing layout features and additional circuitry is used to make measurements from symmetrically-located points. In addition to the normal sense output, self-test outputs are used to detect the presence of layout asymmetry that are caused by local, hard-to-detect defects. Simulation results for an accelerometer reveal that our self-test approach is able to distinguish misbehavior resulting from local defects and global manufacturing process variations. A mathematical model is developed to analyze the efficacy of the differential built-in self-test method in characterization of a wide range of local manufacturing variations affecting different regions of a device and/or wafer. Model predictions are validated by simulation. Specifically, it has been shown that by using a suitable modulation scheme, sensitivity to etch variation along a particular direction is improved by nearly* 30%.

## 1 Introduction

The increasing need for multi-functional sensor and actuator systems that are capable of real-time interaction with both electrical and non-electrical environments has led to the development of a very broad class of "Microsystems". Microsystems are heterogeneous [1] since they are based on the interactions of multiple energy domains that can include electrical, mechanical, optical, thermal, chemical and fluidic. Major classes of microsystems include MicroElectroMechanical Systems (MEMS), MicroOptoElectroMechanical Systems (MOEMS), and MicroElectroFluidic Systems (MEFS). Reliable manufacture of affordable microsystems naturally requires the use of cost-effective test methods that distinguish malfunctioning systems from good ones. The multi-domain nature of microsystems makes them inherently complex for both design and test. In addition, the growing use of microsystems in life-critical applications such as air-bags [2], bio-sensors [3] and satellites [4] creates a significant need for high reliability that cannot be achieved without the use of robust test methods.

Among currently used MEMS process technologies, surface micromachining [5] is widely used due to its similarity to thin-film technology used for integrated circuits. Surface micromachining is already proven to be a technology that is commercially viable since it has supported high-volume manufacture of MEMS devices. Example applications of this technology include the digital micromirror display [6] and the accelerometer [7, 8]. Our work in microsystem test has therefore been focussed on surface-micromachined devices. However, we believe the built-in test method described here is also applicable to other process technologies.

The objective of manufacturing test is to identify malfunctioning devices in a batch of fabricated devices. Device

*This research was sponsored by the National Science Foundation under grant no. MIP-9702678 and the MARCO Gigascale Systems Research Center.

malfunction is caused by various failure sources in the manufacturing process that include but are not limited to foreign particles [9], etch variations and stiction [10, 11], each of which can lead to a variety of defects. When defects cause the device performance to go "out-of-spec", the device is said to have failed. However, test has limitations which can cause good devices to be rejected (yield loss) and bad devices to be accepted (test escape). The cost of test escape can exceed the cost of yield loss since a device that passes traditional, specification-based manufacturing test may fail in the field with catastrophic results [12]. One of the goals of built-in self test (BIST) is the prevention of field failures due to diverse failure sources (see Table 1).

| Failure source | Occurrence in manufacturing | Occurrence in the field |
| --- | --- | --- |
| Foreign particles | yes | yes |
| Etch variations | yes | no |
| Stiction | yes | yes |
| Curvature | yes | yes |

Table 1: Possibility of occurrence of various failure sources during the device lifetime.

Commercially-manufactured MEMS are typically affected by multiple failure sources. Defects caused by many of these failure sources exhibit very similar behaviors [12] which fall within the specified tolerance ranges. Since these similar-behaving defects may have widely varying stability characteristics, those which are unstable over time pose a reliability problem. Therefore, there is a need to distinguish unstable defects from the stable ones. BIST can identify potentially unstable defects [13]. In addition, simultaneously existing multiple failure sources can cause misbehavior masking [12] that often leads to hard-to-detect defects because the misbehavior due to one defect is negated by that caused by another defect. BIST offers a way of detecting hard-to-detect defects [13]. Since the complexity and range of applications of MEMS have grown, off-chip testing has increased in cost, which in turn has enhanced the need for on-chip self-test capability. Current commercial BIST techniques are similar to the one described in [17] and commonly require calibration and therefore are not useful for manufacturing test. Hence, BIST suitable for manufacturing test of MEMS is needed. Previous work [13]-[19] has addressed some of these problems. For example, our work [13, 14, 15] describes a BIST approach that samples outputs from symmetrically-located nodes of the MEMS microstructure. Increasing observability in this way allows one to identify misbehavior resulting from local defects as opposed to more benign causes such as global etch variation.

The work in this paper is a continuation of the differential BIST approach [13, 14, 15] and aims to build a mathematical model for an integrated and comprehensive approach to this form of BIST, when applied to an accelerometer sensor. We show how the BIST can be used to detect the presence of device asymmetry caused by different types of local defects. Simulation results reveal that local defects such as particulates, local over/under-tech, and local curl-mismatch that are not detected by standard specification-based tests, can be detected by our BIST. In addition to self-test, our technique is shown to be useful for device and wafer characterization. Our analyses (theoretical and simulation) validate the claim that the BIST measurements can reveal significant information about the nature of local manufacturing variations affecting different portions of a given die.

The remaining portions of this paper are organized as follows. Section 2 describes a model of the capacitor-based sensing network used in a MEMS accelerometer. Section 3 describes the model developed for representing local manufacturing variations. Section 4 discusses the extent to which each BIST modulation scheme is sensitive to different types of local manufacturing variations. The simulation results for various types of local defects and manufacturing variations are presented in section 5. In section 6, device and wafer characterization using BIST is described. Finally, in section 6, conclusions are drawn based on how sensitive the various modes of BIST are to specific local manufacturing variations in the accelerometer sensor.

## 2 Capacitor Network Model

In this section, we develop an electrical model that represents the network of combdrive capacitors for an accelerometer sensor. Figure 1 illustrates the topology of a CMOS-MEMS accelerometer sensor [23]. The sensor mass is largely provided by the rigid shuttle. The flexible serpentine springs that attach the shuttle to the anchors are made of beams ($B_1$-$B_4$ in Figure 1). The combdrives consist of interdigitated beam-like structures (called "fingers", examples of which are $M_6$ and $F_3$ in Figure 1). Fingers attached to the shuttle are movable while those attached to anchors are fixed. There are other beam-like structures called dummy fingers ($D_1$-$D_8$ in Figure 1) which are manufacture-enhancing features used to achieve the same level of etching for the spring beams and the combdrive fingers. The combdrives are centers of electromechanical interaction. The sense combdrives convert mechanical displacement into electrical voltage/current while the actuation combdrives convert electrical voltage into mechanical force.

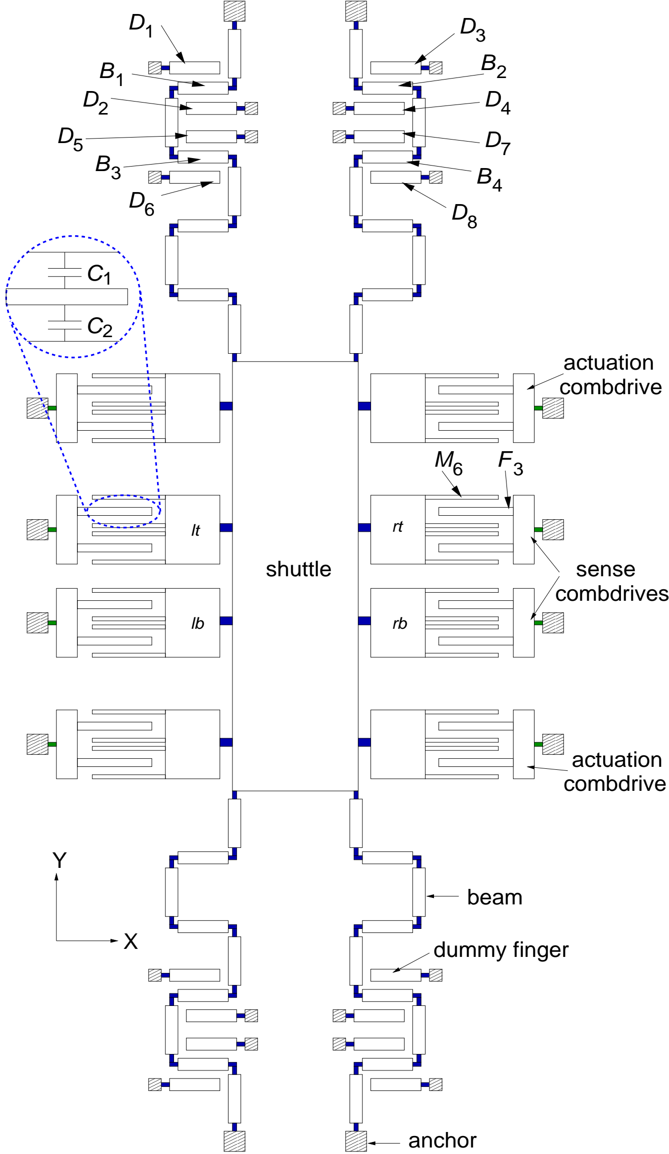


Figure 1: Topology of an accelerometer sensor.

The sense operation is based on the fully differential sensing technique [24] and the sense signals are tapped from the sense combdrives. As shown in Figure 1, the sensor has four identical, symmetrically-located sense combdrives.

A combdrive is electrically represented as a pair of capacitors connected in series (see magnified view of combdrive fingers in Figure 1). Note that each combdrive capacitor, in reality, is an array of capacitors connected in parallel. The circuit network constituted by the capacitors in the four sense combdrives is shown in Figure 2(a). The symbols '$l$', '$r$', '$b$', and '$t$' in Figures 1 and 2 denote left, right, bottom and top, respectively. The subscripts '1' and '2' denote the two capacitors of a differential pair within a combdrive. For example, $C_{1lb}$ is a lumped capacitor that represents the top array of capacitors of the left bottom sense combdrive. For shuttle motion in the $+Y$ direction (see Figure 1), all capacitors with a subscript '1' decrease while all capacitors with a subscript '2' increase. The opposite changes in the capacitance values take place for motion in the $-Y$ direction.

### 2.1 Modulation Schemes

The capacitors in the sensor of Figure 1 can be represented by the equivalent network shown in Figure 2(a) and have the following generic characteristics:

1. Each pair of electrically-connected capacitors constitutes a potential divider circuit. Voltage is applied to each free or *modulation* node of each capacitor and voltage is sensed from their common or *sense* node. Thus, each capacitor pair has one sense node and two modulation nodes.

2. Each pair of capacitors must have different signals ap-

plied to their modulation nodes in order for the sense node to be sensitive to changes in the capacitances. Usually the modulation signals are applied in opposite phases. Therefore each capacitor pair constituting a combdrive can be viewed as a *dipole*[1].

3. The number of modulation *states* associated with each dipole is given by the permutation ${}^{m}P_2 = m(m-1)$, where $m$ is the number of phases of the applied modulation signal, or in general, the number of modulation signals. So, if one of $m$ modulation signals is applied to one modulation node, then there is a choice of $m-1$ signals for the other modulation node.

Note as an aside that these characteristics are applicable to other networks shown in Figure 2 as well.

For the typical choice of $m = 2$, each dipole can have two possible states, denoted by symbols 0 and 1. Every dipole has two capacitors, one labeled with a '1' in the subscript and the other with a '2' in the subscript. If the + phase ($V_{mp}$) of the modulation signal is applied to the free node of the capacitor with subscript '1', then the − phase ($V_{mn}$) of the modulation signal, naturally, is applied to the free node of the capacitor with subscript '2', and the dipole is said to be in state 0. By swapping the modulation signals, the dipole is put in state 1.

A capacitor network consisting of $n$ dipoles can be in $2^n$ modes. However, for the purpose of our analysis, only $n$ suitably-chosen modes are needed for a system of $n$ dipoles. How these $n$ modes are selected is explained next. Since changing the state of each dipole will only change the polarity of the sense output, only $2^{n-1}$ modes out of the total of $2^n$ are uniquely interesting. This number can be further reduced since only the $\frac{{}^{n}C_{n/2}}{2}$ balanced modes (*i.e.*, modes with equal number of 0's and 1's) and the all-zero mode (or its mirror, the all-one mode) are worth analysis because they subsume information captured by the unbalanced modes. Therefore, we only need to choose $n-1$ suitable modes from the set of balanced modes. For our case of $n = 4$, only 4 modes out of a total of 16 need to be examined.

[1] A dipole is defined as an object with opposite polarities at its two ends.

## 2.2 Modal Dependence Relations

The sense voltage outputs $V_A$ and $V_B$ , tapped from nodes $A$ and $B$ ((see Figure 2(a)) respectively, depend on changes in the capacitors of the electrical network shown in Figure 2(a)-(c). In the fully-differential sensing topology [23], the *change* in the voltage difference, $V_B - V_A$, is measured by a differential amplifier (see Figure 3) and is of most interest. For the sake of convenience, the gain of the amplifier has been assumed to be unity. Here, based on electrical network theory, we derive a relation that captures the dependence of $V_B - V_A$ on changes in the network capacitances. All three configurations of fully differential sensing topologies shown in Figure 2(a)-(c) have been known to be usable. We have arbitrarily focussed on the diagonal configuration (see Figure 2(a)) since it is frequently used [24, 23] and because the fundamental conclusions we arrive at are largely independent of the sense configuration chosen.

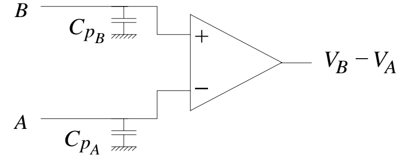


Figure 3: Schematic of a differential amplifier used to measure changes in sense voltage outputs of sense combdrives.

Using the topology of the dipole capacitances ($C_{ji}$, $j \in \{1,2\}, i \in \{lt, rb, lb, rt\}$) illustrated in Figure 2(a) and the parasitic capacitances ($C_{p_A}$ and $C_{p_B}$) shown in Figure 3, the total capacitances at nodes $A$ and $B$ are found to be:

$$C_{A_{total}} = \sum_{i,j} C_{ji} + C_{p_A}, \text{ where } j \in \{1,2\}, i \in \{lt, rb\} \quad (1)$$

$$C_{B_{total}} = \sum_{i,j} C_{ji} + C_{p_B}, \text{ where } j \in \{1,2\}, i \in \{lb, rt\} \quad (2)$$

However, if each dipole capacitance $C_{ji}$ changes to $C'_{ji}$, *e.g.*, due to shuttle displacement), then the corresponding altered values would be:

$$C'_{A_{total}} = \sum_{i,j} C'_{ji} + C_{p_A}, \text{ where } j \in \{1,2\}, i \in \{lt, rb\} \quad (3)$$

$$C'_{B_{total}} = \sum_{i,j} C'_{ji} + C_{p_B}, \text{ where } j \in \{1,2\}, i \in \{lb, rt\} \quad (4)$$

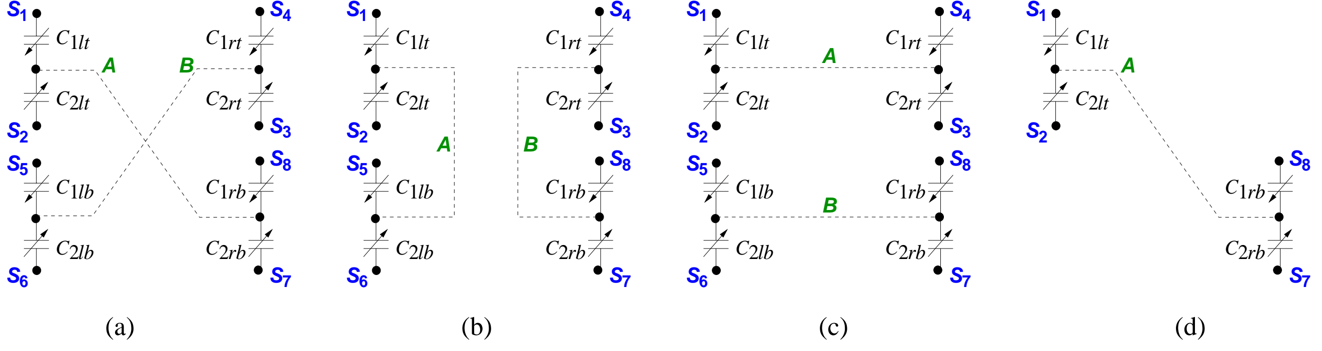


Figure 2: Potential divider circuit formed by a set of sense combdrive capacitors in the fully-differential sensing scheme in (a) diagonal, (b) vertical, (c) horizontal sense configurations and (d) its simplified version, the basic differential sensing scheme. Nodes $A$ and $B$ are sense nodes while $S_1$-$S_8$ are modulation nodes.

We define the change in dipole capacitance as

$$\Delta C_{ji} = C'_{ji} - C_{ji}, \text{ where } j \in \{1,2\}, i \in \{lt, rb, lb, rt\} \tag{5}$$

If we impose the condition that the sum of the capacitances in a dipole is *constant* (for small displacements), then we have the following:

$$C_{1i} + C_{2i} = C'_{1i} + C'_{2i} \Rightarrow \Delta C_{1i} = -\Delta C_{2i}, \text{ where } i \in \{lt, rb, lb, rt\} \tag{6}$$

Substituting Equation 6 into Equations 1-4 leads to the conclusion that

$$C_{A_{total}} = C'_{A_{total}} \tag{7}$$

$$C_{B_{total}} = C'_{B_{total}} \tag{8}$$

Let $V_{ji}$ ($j \in \{1,2\}, i \in \{lt, rb, lb, rt\}$) be the voltage applied to the modulation node of dipole capacitor $Cji$ (see Figure 2(a)). In our analysis $V_{ji} \in \{V_{mp}, V_{mn}\}$ but other values of $V_{ji}$ are also possible. Let $\Delta V_A$ and $\Delta V_B$ be the changes in $V_A$ and $V_B$, respectively, caused by the changes in the dipole capacitances. Hence, from Kirchoff's voltage law, we derive the following relation:

$$\Delta V_A = \sum_{i,j} \frac{C'_{ji} V_{ji}}{C'_{A_{total}}} - \sum_{i,j} \frac{C_{ji} V_{ji}}{C_{A_{total}}} = \sum_{i,j} \left[ \frac{C'_{ji}}{C'_{A_{total}}} - \frac{C_{ji}}{C_{A_{total}}} \right] V_{ji}, \tag{9}$$

$$\text{where } j \in \{1,2\}, i \in \{lt, rb\}$$

Substituting Equation 7 into Equation 10 and then using Equation 5, we have:

$$\Delta V_A = \sum_{i,j} \frac{\Delta C_{ji} V_{ji}}{C_{A_{total}}}, \text{ where } j \in \{1,2\}, i \in \{lt, rb\} \tag{10}$$

Substituting Equation 6 into Equation 10, we get:

$$\begin{aligned} \Delta V_A &= \sum_{i} \frac{\Delta C_{1i}(V_{1i} - V_{2i})}{C_{A_{total}}}, \text{ where } i \in \{lt, rb\} \\ &= \frac{\Delta C_{1lt}(V_{1lt} - V_{2lt}) + \Delta C_{1rb}(V_{1rb} - V_{2rb})}{C_{A_{total}}} \end{aligned} \tag{11}$$

Similarly, we have for $\Delta V_B$:

$$\begin{aligned} \Delta V_B &= \sum_{i,j} \frac{\Delta C_{ji} V_{ji}}{C_{B_{total}}}, \text{ where } j \in \{1,2\}, i \in \{lb, rt\} \\ &= \sum_{i} \frac{\Delta C_{1i}(V_{1i} - V_{2i})}{C_{B_{total}}}, \text{ where } i \in \{lb, rt\} \\ &= \frac{\Delta C_{1lb}(V_{1lb} - V_{2lb}) + \Delta C_{1rt}(V_{1rt} - V_{2rt})}{C_{B_{total}}} \end{aligned} \tag{12}$$

Different modulation signals should be applied to the two free nodes of each dipole. As already mentioned, the two phases of the modulation signal are $V_{mp}$ and $V_{mn}$. Hence, if $V_{1lt} = V_{mp}, V_{2lt} = V_{mn}$, then dipole $lt$ is in state 0. On the other hand, if $V_{1lt} = V_{mn}, V_{2lt} = V_{mp}$, then dipole $lt$ is in state 1. We use $S_{lt} = 1$ and $S_{lt} = -1$ to represent states 0 and 1, respectively, for the dipole $lt$. Similar reasoning applies for all other dipoles. In general, the variable $S_i$ ($i \in \{lt, rb, lb, rt\}$) is used to represent the state of dipole $i$ such that $S_i = 1$, if dipole $i$ is in state 0 and $S_i = -1$, if dipole $i$ is in state 1. Therefore, Equations 11 and 12 reduce to:

$$\Delta V_A = \frac{S_{lt}\Delta C_{1lt} + S_{rb}\Delta C_{1rb}}{C_{A_{total}}}(V_{mp} - V_{mn}) \tag{13}$$

$$\Delta V_B = \frac{S_{lb}\Delta C_{1lb} + S_{rt}\Delta C_{1rt}}{C_{B_{total}}}(V_{mp} - V_{mn}) \tag{14}$$

Subtracting Equation 13 from Equation 14, we get

$$\frac{\Delta V_B - \Delta V_A}{V_{mp} - V_{mn}} = \frac{S_{lb}\Delta C_{1lb} + S_{rt}\Delta C_{1rt}}{C_{B_{total}}} - \frac{S_{lt}\Delta C_{1lt} + S_{rb}\Delta C_{1rb}}{C_{A_{total}}} \tag{15}$$

Equation 15 is the *unified expression for all modes* for the network configuration shown in Figure 2(a).

Equation 11 or 12 is also applicable to basic differential sensing scheme used in devices manufactured from single-conductor processes such as MUMPS [28]. Since the basic differential case uses only one diagonal (sense node A for example) of the network in Figure 2(a), it is reduced to that

shown in Figure 2(d). The change in voltage of the sense node $A$ for this simplified case is obtained by substituting $V_{1lt} = V_{mp}$, $V_{1rb} = V_{mn}$, and $V_{2lt} = V_{2rb} = \frac{V_{mp}+V_{mn}}{2}$ in Equation 11, which then reduces to:

$$\frac{\Delta V_A}{V_{mp} - V_{mn}} = \frac{\Delta C_{1lt} - \Delta C_{1rb}}{2C_{A_{total}}} \tag{16}$$

It is evident from Equation 16 that $\Delta V_A$ is non-zero only when $\Delta C_{1lt} \neq \Delta C_{1rb}$, a condition that implies the presence of an asymmetry/mismatch between the two combdrives concerned.

# 3 Local Manufacturing Variations

Local manufacturing variation is the uncorrelated (mismatch) component of manufacturing variations and is strongly dependent on device layout attributes (length, width, orientation, surrounding topography, *etc.*) [29]. In contrast, global manufacturing variation is the correlated component of manufacturing variations and is therefore independent of device layout attributes. We have focussed on local manufacturing variation since our goal is to detect device asymmetry, of which mismatch is one of the causes.

Dipole capacitance $C_{ji}$ depends on physical parameters such as finger width, the gap between fingers, finger thickness, finger height mismatch, *etc*. All of these parameters may vary over the plane of the device, meaning each is a function of location. In our analyses, each point in the device layout is represented by the coordinates ($\alpha$, $\beta$). Here, we analyze the combined effect of all local manufacturing variations on a dependent variable (*e.g.*, combdrive capacitance) distributed over device area $A$. The dimensionless variable $\lambda(\alpha,\beta)$ represents local manufacturing variations and its impact on combdrive capacitance is characterized as:

$$C_{ji} = C_0 \int_A \lambda(\alpha,\beta) \frac{d\alpha d\beta}{A} \tag{17}$$

In the absence of local manufacturing variations, $\lambda(\alpha,\beta) = 1, \forall\alpha, \forall\beta$, and Equation 17 reduces to the simple relation, $C_{ji} = C_0$. Hence, $C_0$ is the nominal value of $C_{ji}$.

When the sensor moves, $C_{ji}$ changes but $\lambda(\alpha,\beta)$ is assumed to remain constant for small displacements of the microstructures forming the capacitors $C_{ji}$.

The parameter $\lambda(\alpha,\beta)$ can be conveniently expressed as

$$\lambda(\alpha,\beta) = k_{00} + X(\alpha) + Y(\beta) + Z(\alpha,\beta) \tag{18}$$

where $k_{00}$ is a constant, $X(\alpha)$ includes only and all terms that are functions of $\alpha$ alone, $Y(\beta)$ includes only and all terms that are functions of $\beta$ alone, and $Z(\alpha,\beta)$ includes only and all cross-product terms (*i.e.*, functions of both $\alpha$ and $\beta$). The form of Equation 18 reveals that $k_{00} = 1$ if the nominal values $\lambda(0,0) = 1, X(0) = Y(0) = Z(0,0) = 0$ hold true.

Substituting Equation 18 in Equation 17 and assuming that the area $A$ is rectangular and equals $(\alpha_2 - \alpha_1)(\beta_2 - \beta_1)$, we have:

$$\begin{aligned} C_{ji} &= \frac{C_0}{(\alpha_2-\alpha_1)(\beta_2-\beta_1)} \int_{\alpha_1}^{\alpha_2}\int_{\beta_1}^{\beta_2} [k_{00} + X(\alpha) + Y(\beta) + Z(\alpha,\beta)]\, d\alpha d\beta \\ &= C_0 \left[k_{00} + \frac{1}{\alpha_2 - \alpha_1}\int_{\alpha_1}^{\alpha_2} X(\alpha) d\alpha + \frac{1}{\beta_2 - \beta_1}\int_{\beta_1}^{\beta_2} Y(\beta) d\beta\right] \\ &\quad + C_0 \left[\frac{1}{(\alpha_2 - \alpha_1)(\beta_2 - \beta_1)} \int_{\alpha_1}^{\alpha_2}\int_{\beta_1}^{\beta_2} Z(\alpha,\beta) d\alpha d\beta\right] \end{aligned} \tag{19}$$

Using the Mean Value Theorem of calculus, it can be shown that there exists a location $(\alpha_0, \beta_0)$ within the rectangle area $A$ such that:

$$X(\alpha_0) = \frac{1}{\alpha_2 - \alpha_1}\int_{\alpha_1}^{\alpha_2} X(\alpha) d\alpha \tag{20}$$

$$Y(\beta_0) = \frac{1}{\beta_2 - \beta_1}\int_{\beta_1}^{\beta_2} Y(\beta) d\beta \tag{21}$$

Equations 20-21 can be used to simplify Equation 19 to:

$$C_{ji} = C_0 \left[k_{00} + X(\alpha_0) + Y(\beta_0) + Z_{avg}\right] \tag{22}$$

where

$$Z_{avg} = \frac{1}{(\alpha_2 - \alpha_1)(\beta_2 - \beta_1)} \int_{\alpha_1}^{\alpha_2}\int_{\beta_1}^{\beta_2} Z(\alpha,\beta) d\alpha d\beta \tag{23}$$

Equation 22 captures the concept of average manufacturing variations. Since the combdrive capacitance is distributed over an area, the combined effect of all manufacturing variations over the area is equated to an average multiplied by the same area. The fact that only one sense signal comes out of the entire combdrive/dipole imposes a practical limit on resolving local variations that are internal to the combdrive. Hence, we will use the average value ($\lambda_{avg}$) to represent the distributed dipole capacitance. Therefore, from Equations 17 and 22, it is evident that

$$\frac{C_{ji}}{C_0} = \lambda_{avg} = k_{00} + X(\alpha_0) + Y(\beta_0) + Z_{avg} \tag{24}$$

Equation 24 indicates that the average manufacturing variation in a quadrant can be represented by the value of $\lambda$ at a single point in the quadrant. Therefore, the point locations $(\alpha^+, \beta^+)$ and $(\alpha^-, \beta^-)$ are assigned to the combdrives in two diagonally opposite quadrants, right-top (*rt*) and left-bottom (*lb*), respectively. Hence, we have from Equation 24 for the *rt* quadrant:

$$\frac{C_{1rt}}{C_0} = \frac{C_{2rt}}{C_0} = \lambda_{rt} = k_{00} + X(\alpha^+) + Y(\beta^+) + Z_{rt} \tag{25}$$

where

$$X(\alpha^+) = \frac{1}{\alpha_2 - \alpha_1} \int_{\alpha_1}^{\alpha_2} X(\alpha) d\alpha \tag{26}$$

$$Y(\beta^+) = \frac{1}{\beta_2 - \beta_1} \int_{\beta_1}^{\beta_2} Y(\beta) d\beta \tag{27}$$

$$Z_{rt} = \frac{1}{A} \int_{\beta_1}^{\beta_2} \int_{\alpha_1}^{\alpha_2} Z(\alpha, \beta) d\alpha d\beta \tag{28}$$

Similarly, Equation 24 gives the following relations for the *lb* quadrant:

$$\frac{C_{1lb}}{C_0} = \frac{C_{2lb}}{C_0} = \lambda_{lb} = k_{00} + X(\alpha^-) + Y(\beta^-) + Z_{lb} \tag{29}$$

where

$$X(\alpha^-) = \frac{1}{(-\alpha_1) - (-\alpha_2)} \int_{-\alpha_2}^{-\alpha_1} X(\alpha) d\alpha = \frac{1}{\alpha_2 - \alpha_1} \int_{\alpha_1}^{\alpha_2} X(-\alpha) d\alpha \tag{30}$$

$$Y(\beta^-) = \frac{1}{(-\beta_1) - (-\beta_2)} \int_{-\beta_2}^{-\beta_1} Y(\beta) d\beta = \frac{1}{\beta_2 - \beta_1} \int_{\beta_1}^{\beta_2} Y(-\beta) d\beta \tag{31}$$

$$Z_{lb} = \frac{1}{A} \int_{-\beta_2}^{-\beta_1} \int_{-\alpha_2}^{-\alpha_1} Z(\alpha, \beta) d\alpha d\beta = \frac{1}{A} \int_{\beta_1}^{\beta_2} \int_{\alpha_1}^{\alpha_2} Z(-\alpha, -\beta) d\alpha d\beta \tag{32}$$

It follows from Equations 26, 27, 30, and 31 that for the combdrives in the other two quadrants, left-top (*lt*):

$$\frac{C_{1lt}}{C_0} = \frac{C_{2lt}}{C_0} = \lambda_{lt} = k_{00} + X(\alpha^-) + Y(\beta^+) + Z_{lt} \tag{33}$$

where

$$Z_{lt} = \frac{1}{A} \int_{\beta_1}^{\beta_2} \int_{-\alpha_2}^{-\alpha_1} Z(\alpha, \beta) d\alpha d\beta = \frac{1}{A} \int_{\beta_1}^{\beta_2} \int_{\alpha_1}^{\alpha_2} Z(-\alpha, \beta) d\alpha d\beta \tag{34}$$

and right-bottom (*rb*):

$$\frac{C_{1rb}}{C_0} = \frac{C_{2rb}}{C_0} = \lambda_{rb} = k_{00} + X(\alpha^+) + Y(\beta^-) + Z_{rb} \tag{35}$$

where

$$Z_{rb} = \frac{1}{A} \int_{-\beta_2}^{-\beta_1} \int_{\alpha_1}^{\alpha_2} Z(\alpha, \beta) d\alpha d\beta = \frac{1}{A} \int_{\beta_1}^{\beta_2} \int_{\alpha_1}^{\alpha_2} Z(\alpha, -\beta) d\alpha d\beta \tag{36}$$

Equations 25, 29, 33, and 35 represent the dependence of the combdrive capacitances on the average local manufacturing variations in each quadrant and will be used for later analyses.

For the purpose of a more detailed analysis, which will show how various BIST modes are sensitive (or insensitive) to manufacturing variations along specific directions in the device plane, we now express $\lambda(\alpha, \beta)$ as a two-dimensional power series of $\alpha$ and $\beta$ as follows:

$$\lambda(\alpha, \beta) = \sum_{m=0,n=0}^{\infty,\infty} k_{mn} \alpha^m \beta^n \tag{37}$$

where $k_{mn}$ (sometimes also written as $k_{m,n}$ for clarity) are constant coefficients. From Equation 37 and prior definitions of $X(\alpha)$, $Y(\beta)$, and $Z(\alpha, \beta)$ in Equation 18, it follows that:

$$X(\alpha) = \sum_{m=1}^{\infty} k_{m0} \alpha^m \tag{38}$$

$$Y(\beta) = \sum_{n=1}^{\infty} k_{0n} \beta^n \tag{39}$$

$$Z(\alpha, \beta) = \sum_{m=1,n=1}^{\infty,\infty} k_{mn} \alpha^m \beta^n \tag{40}$$

Note as an aside from Equations 38-40 that if $k_{mn} = k_{m0} k_{0n}$ (for all $m \geq 1, n \geq 1$), then $Z(\alpha, \beta) = X(\alpha) Y(\beta)$. This condition leads to the special case (already analyzed in [14]) where $\lambda(\alpha, \beta) = [1 + X(\alpha)][1 + Y(\beta)]$ is variable separable.

Substituting Equation 37 into Equation 17 gives the following expression for $C_{ji}$:

$$\begin{aligned}
C_{ji} &= C_0 \frac{1}{A} \int_A \lambda(\alpha, \beta) d\alpha d\beta = C_0 \frac{1}{A} \int_A \sum_{m=0,n=0}^{\infty,\infty} k_{mn} \alpha^m \beta^n d\alpha d\beta \\
&= C_0 \frac{1}{A} \sum_{m=0,n=0}^{\infty,\infty} k_{mn} \int_A \alpha^m \beta^n d\alpha d\beta, [A = (\alpha_2 - \alpha_1)(\beta_2 - \beta_1)] \\
&= C_0 \frac{1}{(\alpha_2 - \alpha_1)(\beta_2 - \beta_1)} \sum_{m=0,n=0}^{\infty,\infty} k_{mn} \int_{\alpha_1}^{\alpha_2} \int_{\beta_1}^{\beta_2} \alpha^m \beta^n d\alpha d\beta \\
&= C_0 \frac{1}{(\alpha_2 - \alpha_1)(\beta_2 - \beta_1)} \sum_{m=0,n=0}^{\infty,\infty} k_{mn} \int_{\alpha_1}^{\alpha_2} \alpha^m d\alpha \int_{\beta_1}^{\beta_2} \beta^n d\beta \\
&= C_0 \sum_{m=0,n=0}^{\infty,\infty} u_{mn}
\end{aligned} \tag{41}$$

where $u_{mn}$ is a constant given by:

$$u_{mn} = \frac{k_{mn}}{(m+1)(n+1)} \cdot \frac{(\alpha_2^{m+1} - \alpha_1^{m+1})(\beta_2^{n+1} - \beta_1^{n+1})}{(\alpha_2 - \alpha_1)(\beta_2 - \beta_1)} \tag{42}$$

From Equation 42, it is obvious that:

$$u_{00} = k_{00} \tag{43}$$

$$u_{m0} = \frac{1}{\alpha_2 - \alpha_1} \cdot \frac{k_{m0}}{m+1} (\alpha_2^{m+1} - \alpha_1^{m+1}), m \geq 1 \tag{44}$$

$$u_{0n} = \frac{1}{\beta_2 - \beta_1} \cdot \frac{k_{0n}}{n+1} (\beta_2^{n+1} - \beta_1^{n+1}), n \geq 1 \tag{45}$$

$$u_{mn} = u_{m0} \cdot u_{0n} \cdot \frac{k_{mn}}{k_{m0} \cdot k_{0n}} \tag{46}$$

Substituting Equation 38 in Equations 26 and 30, and then simplifying using Equation 44, we get

$$X(\alpha^+) = \sum_{m=1}^{\infty} u_{m0} \ , \quad X(\alpha^-) = \sum_{m=1}^{\infty} u_{m0}(-1)^m \tag{47}$$

Similarly, substituting Equation 39 in Equations 27 and 31, and then simplifying using Equation 45, we get

$$Y(\beta^+) = \sum_{n=1}^{\infty} u_{0n} \ , \quad Y(\beta^-) = \sum_{n=1}^{\infty} u_{0n}(-1)^n \tag{48}$$

Also, Equation 40 is substituted into Equations 28, 32, 34 and 36, and then simplified using Equation 42 to give

$$Z_{rt} = \sum_{m=1,n=1}^{\infty,\infty} u_{mn} \ , \quad Z_{lb} = \sum_{m=1,n=1}^{\infty,\infty} u_{mn}(-1)^{m+n} \tag{49}$$

$$Z_{lt} = \sum_{m=1,n=1}^{\infty,\infty} u_{mn}(-1)^m \ , \quad Z_{rb} = \sum_{m=1,n=1}^{\infty,\infty} u_{mn}(-1)^n \tag{50}$$

The relations described by Equations 47-50 will be used to calculate the sensitivities of the BIST modes.

# 4 BIST Mode Sensitivity Analyses

Here, we analyze how the sense combdrive capacitors, under different modulation schemes, produce a sense signal that may or may not depend on first-order[2] local manufacturing variations, device rotation, DC offset, and combdrive configuration.

## 4.1 Impact of Mismatch

In the presence of local manufacturing variations, the dipole capacitors have these values for zero shuttle displacement:

$$C_{ji} = C_0\lambda_i, \text{ where } i \in \{lt, rb, lb, rt\}, j \in \{1,2\}. \tag{51}$$

When the shuttle is displaced, the expressions for the combdrive capacitors change to:

$$C'_{1i} = C_0\lambda_i + \Delta C_{1i}, i \in \{lt, rb, lb, rt\} \tag{52}$$

$$C'_{2i} = C_0\lambda_i + \Delta C_{2i}, i \in \{lt, rb, lb, rt\} \tag{53}$$

where

$$\Delta C_{1i} = -\Delta C_{2i} = -\delta \cdot \lambda_i \cdot \phi_i, i \in \{lt, rb, lb, rt\} \tag{54}$$

The quantity $\Delta C_{1i}$ (in Equation 54) depends on both the local variations in the combdrive as well as the displacement of the movable part of the combdrive. We assume that $\lambda_i$ ($i \in \{rt, lb, lt, rb\}$) remains constant for small displacements ($|\Delta C_{1i}/C_0| \ll 1$) of the microstructure. Therefore, $\Delta C_{1i}$ and $C_{1i}$ have the same dependence on local variations in the combdrive. Hence, the dependence of $\Delta C_{1i}$ on local variations in the combdrive alone is represented by $\lambda_i$ in Equation 54. In addition, the combdrive displacement in each quadrant depends on the effect of local manufacturing variations on other structures, such as beams and plates. Hence, an additional quantity $\phi_i$ ($i \in \{rt, lb, lt, rb\}$), that includes the indirect effect on combdrive capacitance of local variations affecting other structures (such as beams and plates), appears in Equation 54. In absence of any local manufacturing variations in the beams and the plates, $\phi_i = 1$. Theoretically, in a quadrant $i$, it is possible to have $\lambda_i = 1$ (no local variations in the combdrive) and $\phi_i \neq 1$ (local variations in the beams and plates). Under such conditions, the undisplaced combdrive capacitors have the nominal value ($C_{1i} = C_{2i} = C_0$ from Equation 51) but during displacement, $\Delta C_{1i} = -\delta\phi_i \neq -\delta$ (from Equation 54), which is expected since the combdrive displacement is not nominal. Now, for the sake of convenience, the term $\phi_i$ can be absorbed into $\lambda_i$ so that from now on it is understood that $\lambda_i$ includes the effect of local variations on all structures (combdrives, beams, plates, *etc.*) in quadrant $i$. Therefore, Equation 54 reduces to:

$$\Delta C_{1i} = -\Delta C_{2i} = -\delta\lambda_i, i \in \{lt, rb, lb, rt\}. \tag{55}$$

From Equation 55, we have $\Delta C_{1lt} = -\delta\lambda_{lt}$, $\Delta C_{1rb} = -\delta\lambda_{rb}$, $\Delta C_{1lb} = -\delta\lambda_{lb}$, and $\Delta C_{1rt} = -\delta\lambda_{rt}$. Combining Equation 51 and Equations 1- 2, we have $C_{A_{total}} = 2C_0(\lambda_{lt} + \lambda_{rb}) + C_{p_A}$ and $C_{B_{total}} = 2C_0(\lambda_{lb} + \lambda_{rt}) + C_{p_B}$. Substitution of these values in Equation 15 gives

$$\frac{\Delta V_B - \Delta V_A}{V_{mp} - V_{mn}} = \delta\left[\frac{S_{lt}\lambda_{lt} + S_{rb}\lambda_{rb}}{2C_0(\lambda_{lt} + \lambda_{rb}) + C_{p_A}} - \frac{S_{lb}\lambda_{lb} + S_{rt}\lambda_{rt}}{2C_0(\lambda_{lb} + \lambda_{rt}) + C_{p_B}}\right] \tag{56}$$

$$= \delta \cdot F(S_{lt}, S_{rb}, S_{lb}, S_{rt}) \tag{57}$$

where $F$ is given by

$$F(x_1, x_2, x_3, x_4) = \frac{x_1\lambda_{lt} + x_2\lambda_{rb}}{2C_0(\lambda_{lt} + \lambda_{rb}) + C_{p_A}} - \frac{x_3\lambda_{lb} + x_4\lambda_{rt}}{2C_0(\lambda_{lb} + \lambda_{rt}) + C_{p_B}} \tag{58}$$

Equation 56 allows us to represent the modes of the capacitor network (shown in Figure 2(a)) in the form of a truth table (see Table 2). Every row in Table 2 corresponds to a mode of the capacitor network.

Using Equations 47-48, we define the quantities:

[2] The first-order dependence of variable $y$ on variable $x$ is $\left[\frac{dy}{dx}\right]_{x=0}$.

| Mode | Dipole modulation voltages | | | | Normalized sense output | Mode name |
|---|---|---|---|---|---|---|
| $(lt.rb.lb.rt)$ | $C_{1lt}:C_{2lt}$ | $C_{1rb}:C_{2rb}$ | $C_{1lb}:C_{2lb}$ | $C_{1rt}:C_{2rt}$ | $=(\Delta V_B-\Delta V_A)/(V_{mp}-V_{mn})$ | |
| 0011 | $V_{mp}:V_{mn}$ | $V_{mp}:V_{mn}$ | $V_{mn}:V_{mp}$ | $V_{mn}:V_{mp}$ | $\delta\frac{\lambda_{lt}+\lambda_{rb}}{2C_0(\lambda_{lt}+\lambda_{rb})+C_{pA}}+\delta\frac{\lambda_{lb}+\lambda_{rt}}{2C_0(\lambda_{lb}+\lambda_{rt})+C_{pB}}$ | Normal sense mode |
| 0110 | $V_{mp}:V_{mn}$ | $V_{mn}:V_{mp}$ | $V_{mn}:V_{mp}$ | $V_{mp}:V_{mn}$ | $\delta\frac{\lambda_{lt}-\lambda_{rb}}{2C_0(\lambda_{lt}+\lambda_{rb})+C_{pA}}+\delta\frac{\lambda_{lb}-\lambda_{rt}}{2C_0(\lambda_{lb}+\lambda_{rt})+C_{pB}}$ | Self-test X-mode |
| 0101 | $V_{mp}:V_{mn}$ | $V_{mn}:V_{mp}$ | $V_{mp}:V_{mn}$ | $V_{mn}:V_{mp}$ | $\delta\frac{\lambda_{lt}-\lambda_{rb}}{2C_0(\lambda_{lt}+\lambda_{rb})+C_{pA}}-\delta\frac{\lambda_{lb}-\lambda_{rt}}{2C_0(\lambda_{lb}+\lambda_{rt})+C_{pB}}$ | Self-test Y-mode |
| 0000 | $V_{mp}:V_{mn}$ | $V_{mp}:V_{mn}$ | $V_{mp}:V_{mn}$ | $V_{mp}:V_{mn}$ | $\delta\frac{\lambda_{lt}+\lambda_{rb}}{2C_0(\lambda_{lt}+\lambda_{rb})+C_{pA}}-\delta\frac{\lambda_{lb}+\lambda_{rt}}{2C_0(\lambda_{lb}+\lambda_{rt})+C_{pB}}$ | Self-test XY-mode |

Table 2: Expressions for sense output voltage of various modes of the capacitor network of Figure 2(a) in presence of local manufacturing variations.

$$X_d = X(\alpha^+) - X(\alpha^-) = \sum_{m=1}^{\infty} u_{m0}[1-(-1)^m] = 2\sum_{m=0}^{\infty} u_{2m+1,0} \quad (59)$$

$$Y_d = Y(\beta^+) - Y(\beta^-) = \sum_{n=1}^{\infty} u_{0n}[1-(-1)^n] = 2\sum_{n=0}^{\infty} u_{0,2n+1} \quad (60)$$

$$X_s = X(\alpha^+) + X(\alpha^-) = \sum_{m=1}^{\infty} u_{m0}[1+(-1)^m] = 2\sum_{m=1}^{\infty} u_{2m,0} \quad (61)$$

$$Y_s = Y(\beta^+) + Y(\beta^-) = \sum_{n=1}^{\infty} u_{0n}[1+(-1)^n] = 2\sum_{n=1}^{\infty} u_{0,2n} \quad (62)$$

where $X_d$ ($Y_d$) is a measure of the difference in the level of local manufacturing variations between the left (bottom) and right (top) halves of the device and $X_s$ ($Y_s$) represents the average local manufacturing variations along the $X$ ($Y$) direction.

In addition, using Equations 59-62, the following four variables are defined for the sake of convenience:

$$J_{2m,2n} = \sum_{m=0,n=0}^{\infty,\infty} u_{2m,2n} = \left[1+\frac{X_s}{2}\right]\left[1+\frac{Y_s}{2}\right] + \sum_{m=1,n=1}^{\infty,\infty} u_{2m,2n}\left[1-\frac{k_{0,2n}\cdot k_{2m,0}}{k_{2m,2n}}\right] \quad (63)$$

$$J_{2m+1,2n+1} = \sum_{m=0,n=0}^{\infty,\infty} u_{2m+1,2n+1} = \frac{X_d Y_d}{4} + \sum_{m=0,n=0}^{\infty,\infty} u_{2m+1,2n+1}\left[1-\frac{k_{0,2n+1}\cdot k_{2m+1,0}}{k_{2m+1,2n+1}}\right] \quad (64)$$

$$J_{2m+1,2n} = \sum_{m=0,n=0}^{\infty,\infty} u_{2m+1,2n} = \frac{X_d}{2}\left[1+\frac{Y_s}{2}\right] + \sum_{m=0,n=1}^{\infty,\infty} u_{2m+1,2n}\left[1-\frac{k_{0,2n}\cdot k_{2m+1,0}}{k_{2m+1,2n}}\right] \quad (65)$$

$$J_{2m,2n+1} = \sum_{m=0,n=0}^{\infty,\infty} u_{2m,2n+1} = \frac{Y_d}{2}\left[1+\frac{X_s}{2}\right] + \sum_{m=1,n=0}^{\infty,\infty} u_{2m,2n+1}\left[1-\frac{k_{0,2n+1}\cdot k_{2m,0}}{k_{2m,2n+1}}\right] \quad (66)$$

Substituting Equations 63-66 in Equations 25,29, 33, and 35, we get these sums and differences:

$$\lambda_{lt}+\lambda_{rb} = \sum_{m=0,n=0}^{\infty,\infty} u_{mn}[(-1)^m+(-1)^n] = \sum_{m=0,n=0}^{\infty,\infty} 2[u_{2m,2n}-u_{2m+1,2n+1}] = 2[J_{2m,2n}-J_{2m+1,2n+1}] \quad (67)$$

$$\lambda_{lb}+\lambda_{rt} = \sum_{m=0,n=0}^{\infty,\infty} u_{mn}[(-1)^{m+n}+1] = \sum_{m=0,n=0}^{\infty,\infty} 2[u_{2m,2n}+u_{2m+1,2n+1}] = 2[J_{2m,2n}+J_{2m+1,2n+1}] \quad (68)$$

$$(\lambda_{lt}+\lambda_{rb})+(\lambda_{lb}+\lambda_{rt}) = 4J_{2m,2n} \quad (69)$$

$$(\lambda_{lt}+\lambda_{rb})-(\lambda_{lb}+\lambda_{rt}) = -4J_{2m+1,2n+1} \quad (70)$$

$$\lambda_{lt}-\lambda_{rb} = 2[J_{2m,2n+1}-J_{2m+1,2n}] \quad (71)$$

$$\lambda_{lb}-\lambda_{rt} = -2[J_{2m,2n+1}+J_{2m+1,2n}] \quad (72)$$

$$(\lambda_{lt}-\lambda_{rb})-(\lambda_{lb}-\lambda_{rt}) = 4J_{2m,2n+1} \quad (73)$$

$$(\lambda_{lt}-\lambda_{rb})+(\lambda_{lb}-\lambda_{rt}) = -4J_{2m+1,2n} \quad (74)$$

For simplicity, we assume equal parasitic capacitance, *i.e.*, $C_{p_A}=C_{p_B}=C_p$, and define the following quantities for the sake of developing compact expressions.

$$\mu = \frac{C_p}{4C_0} \quad (75)$$

$$H_{mn} = \frac{1}{4}[\lambda_{lb}+\lambda_{rt}+2\mu][\lambda_{lt}+\lambda_{rb}+2\mu] = [\mu+J_{2m,2n}]^2 - J_{2m+1,2n+1}^2 \quad (76)$$

Substituting Equations 25, 29, 33, and 35 into Equation 56 and then simplifying with the expressions of Equations 63-76 gives the differential sense output for various modes as tabulated in Table 3.

Several special cases can be identified:

1. For odd[3] variation along $X$ direction, $X(-\alpha) = -X(\alpha)$. Imposing this condition in Equation 61 leads to $X_s = 0$.
2. For odd variation along $Y$ direction, $Y(-\beta) = -Y(\beta)$.

[3] $f(x)$ is said to be an odd function of $x$ if $f(-x) = -f(x)$.

| Mode ($lt.rb.lb.rt$) | Normalized sense output $= (\Delta V_B - \Delta V_A)/(V_{mp} - V_{mn})$ |
|---|---|
| 0011 | $\frac{\delta}{C_0}\frac{1}{H_{mn}}\left[J_{2m,2n}\left(\mu + J_{2m,2n}\right) - J^2_{2m+1,2n+1}\right]$ |
| 0110 | $\frac{\delta}{C_0}\frac{1}{H_{mn}}\left[-J_{2m+1,2n}\left(\mu + J_{2m,2n}\right) + J_{2m,2n+1}\cdot J_{2m+1,2n+1}\right]$ |
| 0101 | $\frac{\delta}{C_0}\frac{1}{H_{mn}}\left[J_{2m,2n+1}\left(\mu + J_{2m,2n}\right) - J_{2m+1,2n}\cdot J_{2m+1,2n+1}\right]$ |
| 0000 | $\frac{\delta}{C_0}\frac{\mu}{H_{mn}}\left[-J_{2m+1,2n+1}\right]$ |

Table 3: Changes in sense voltage outputs for various modes of accelerometer sensor operation, after simplifications based on expressions in Table 2.

Imposing this condition in Equation 62 leads to $Y_s = 0$.

Therefore, when $X(\alpha)$ and $Y(\beta)$ are odd functions, Equations 63-66 and Equation 76 reduce to:

$$J_{2m,2n}=1+\sum_{m=1,n=1}^{\infty,\infty} u_{2m,2n}\left[1-\frac{k_{0,2n}\cdot k_{2m,0}}{k_{2m,2n}}\right]\approx 1$$

$$J_{2m+1,2n+1}=\frac{X_dY_d}{4}+\sum_{m=0,n=0}^{\infty,\infty} u_{2m+1,2n+1}\left[1-\frac{k_{0,2n+1}\cdot k_{2m+1,0}}{k_{2m+1,2n+1}}\right]\approx\frac{X_dY_d}{4}$$

$$J_{2m+1,2n}=\frac{X_d}{2}+\sum_{m=0,n=1}^{\infty,\infty} u_{2m+1,2n}\left[1-\frac{k_{0,2n}\cdot k_{2m+1,0}}{k_{2m+1,2n}}\right]\approx\frac{X_d}{2}$$

$$J_{2m,2n+1}=\frac{Y_d}{2}+\sum_{m=1,n=0}^{\infty,\infty} u_{2m,2n+1}\left[1-\frac{k_{0,2n+1}\cdot k_{2m,0}}{k_{2m,2n+1}}\right]\approx\frac{Y_d}{2}$$

$$H_{mn}\approx[1+\mu]^2-\left[\frac{X_dY_d}{4}\right]^2\approx[1+\mu]^2$$

The cross-product terms have been neglected. In addition, $X_d$ and $Y_d$ (defined in Equation 59-60) are much smaller than unity for a normal manufacturing process so that $\left[\frac{X_dY_d}{4}\right]^2 \ll 1$. Under such conditions, the expressions of mode sensitivities in Table 3 reduce to the ones listed in Table 4. Table 4 reveals how local manufacturing variations affect various mode sensitivities and how modes can be used to estimate manufacturing variations along specific directions in the device layout.

## 4.2 Rotation

In-plane rotation of the device causes the capacitors in diagonally-located combs to either increase or decrease. For example, if $C_{lb}$ and $C_{rt}$ increase, $C_{lt}$ and $C_{rb}$ will decrease. If the change in capacitance of one combdrive due to rotation alone is $\delta_{rot}$, from Equations 13 and 14, we have these sense voltages in presence of both translation and rotation:

$$\Delta V_A=-(\delta+\delta_{rot})\frac{S_{lt}\lambda_{lt}+S_{rb}\lambda_{rb}}{2C_0(\lambda_{lt}+\lambda_{rb})+C_{p_A}}(V_{mp}-V_{mn}) \quad (77)$$

$$\Delta V_B=-(\delta-\delta_{rot})\frac{S_{lb}\lambda_{lb}+S_{rt}\lambda_{rt}}{2C_0(\lambda_{lb}+\lambda_{rt})+C_{p_B}}(V_{mp}-V_{mn}) \quad (78)$$

Combining Equations 77 and 78, we have:

$$\begin{aligned}\frac{\Delta V_B-\Delta V_A}{V_{mp}-V_{mn}} &=(\delta+\delta_{rot})\frac{S_{lt}\lambda_{lt}+S_{rb}\lambda_{rb}}{2C_0(\lambda_{lt}+\lambda_{rb})+C_{p_A}}-(\delta-\delta_{rot})\frac{S_{lb}\lambda_{lb}+S_{rt}\lambda_{rt}}{2C_0(\lambda_{lb}+\lambda_{rt})+C_{p_B}}\\ &=\delta\left[\frac{S_{lt}\lambda_{lt}+S_{rb}\lambda_{rb}}{2C_0(\lambda_{lt}+\lambda_{rb})+C_{p_A}}-\frac{S_{lb}\lambda_{lb}+S_{rt}\lambda_{rt}}{2C_0(\lambda_{lb}+\lambda_{rt})+C_{p_B}}\right]\\ &\quad+\delta_{rot}\left[\frac{S_{lt}\lambda_{lt}+S_{rb}\lambda_{rb}}{2C_0(\lambda_{lt}+\lambda_{rb})+C_{p_A}}+\frac{S_{lb}\lambda_{lb}+S_{rt}\lambda_{rt}}{2C_0(\lambda_{lb}+\lambda_{rt})+C_{p_B}}\right] \end{aligned} \quad (79)$$

Using Equation 58, Equation 79 can be represented as

$$\frac{\Delta V_B-\Delta V_A}{V_{mp}-V_{mn}}=\delta\cdot F(S_{lt},S_{rb},S_{lb},S_{rt})+\delta_{rot}\cdot F(S_{lt},S_{rb},-S_{lb},-S_{rt}) \quad (80)$$

Equation 80 reveals that this a mixed-mode case, which is equivalent to two different modes being active simultaneously. Basically, if the externally applied mode is $M = abcd$, an internally generated mode due to rotation will be $M_{rot} = ab\bar{c}\bar{d}$ or $M_{rot} = \bar{a}\bar{b}cd$. Hence, the combined effect is a linear superposition of modes, $M + M_{rot}$. The two modes may reinforce each other or oppose each other, depending on their relative magnitudes and signs. Thus, the effect of in-plane rotation can be captured by using the principle of linear superposition.

Out-of-plane rotation/curvature usually causes all comb capacitances involved to decrease. Hence, it can be modeled as any other manufacturing variation.

## 4.3 DC Offset

DC offset can originate from the sensor microstructure or the pre-amplifier (see Figure 3). A device can be affected by either or both offsets. Using Equation 56, we have shown in [30] that both offsets can be eliminated and (optionally) estimated using $2n$ number of modes , where $n$ is the number of dipoles in the sensor.

| Mode ($lt.rb.lb.rt$) | Normalized sense output $= (\Delta V_B - \Delta V_A)/(V_{mp} - V_{mn})$ | Dependence on manufacturing variations |
|---|---|---|
| 0011 | $\frac{\delta}{C_0}\left[\frac{1}{1+\frac{C_p}{4C_0}}\right]$ | Independent of X and Y variations |
| 0110 | $\frac{\delta}{2C_0}(-X_d)\left[\frac{1+\frac{C_p}{4C_0}-\frac{1}{4}Y_d^2}{(1+\frac{C_p}{4C_0})^2}\right]$ | X variations only (to 1st order), *i.e*, variations between left and right halves |
| 0101 | $\frac{\delta}{2C_0}(+Y_d)\left[\frac{1+\frac{C_p}{4C_0}-\frac{1}{4}X_d^2}{(1+\frac{C_p}{4C_0})^2}\right]$ | Y variations only (to 1st order), *i.e*, variations between top and bottom halves |
| 0000 | $\frac{\delta}{4C_0}(-X_dY_d)\left[\frac{\frac{C_p}{4C_0}}{(1+\frac{C_p}{4C_0})^2}\right]$ | Diagonal variations, *i.e*, variations between the diagonal formed by quadrants [lt, rb] and the diagonal formed by quadrants [lb, rt] |

Table 4: Changes in sense voltage outputs, as obtained by simplifying the expressions in Table 3, for various modes of accelerometer operation (in diagonal sense configuration) and their relationship to specific types of manufacturing variations.

| Mode ($lt.rb.lb.rt$) | **Normalized sense output** $= (\Delta V_B - \Delta V_A)/(V_{mp} - V_{mn})$ | |
|---|---|---|
| | Horizontal | Vertical |
| 0011 | $\delta\frac{\lambda_{lb}-\lambda_{rb}}{2C_0(\lambda_{lb}+\lambda_{rb})+C_p}+\delta\frac{\lambda_{lt}-\lambda_{rt}}{2C_0(\lambda_{lt}+\lambda_{rt})+C_p}$ | $\delta\frac{-\lambda_{lb}+\lambda_{lt}}{2C_0(\lambda_{lb}+\lambda_{lt})+C_p}-\delta\frac{\lambda_{rb}-\lambda_{rt}}{2C_0(\lambda_{rb}+\lambda_{rt})+C_p}$ |
| 0110 | $\delta\frac{\lambda_{lb}+\lambda_{rb}}{2C_0(\lambda_{lb}+\lambda_{rb})+C_p}+\delta\frac{\lambda_{lt}+\lambda_{rt}}{2C_0(\lambda_{lt}+\lambda_{rt})+C_p}$ | $\delta\frac{-\lambda_{lb}+\lambda_{lt}}{2C_0(\lambda_{lb}+\lambda_{lt})+C_p}+\delta\frac{\lambda_{rb}-\lambda_{rt}}{2C_0(\lambda_{rb}+\lambda_{rt})+C_p}$ |
| 0101 | $\delta\frac{-\lambda_{lb}+\lambda_{rb}}{2C_0(\lambda_{lb}+\lambda_{rb})+C_p}+\delta\frac{\lambda_{lt}-\lambda_{rt}}{2C_0(\lambda_{lt}+\lambda_{rt})+C_p}$ | $\delta\frac{\lambda_{lb}+\lambda_{lt}}{2C_0(\lambda_{lb}+\lambda_{lt})+C_p}+\delta\frac{\lambda_{rb}+\lambda_{rt}}{2C_0(\lambda_{rb}+\lambda_{rt})+C_p}$ |
| 0000 | $-\delta\frac{\lambda_{lb}+\lambda_{rb}}{2C_0(\lambda_{lb}+\lambda_{rb})+C_p}+\delta\frac{\lambda_{lt}+\lambda_{rt}}{2C_0(\lambda_{lt}+\lambda_{rt})+C_p}$ | $\delta\frac{\lambda_{lb}+\lambda_{lt}}{2C_0(\lambda_{lb}+\lambda_{lt})+C_p}-\delta\frac{\lambda_{rb}+\lambda_{rt}}{2C_0(\lambda_{rb}+\lambda_{rt})+C_p}$ |

Table 5: Mode sensitivities for horizontal and vertical sense configurations.

## 4.4 Different Network Configurations

Our previous analyses are applicable to a specific type of configuration, where combdrive pairs are electrically connected diagonally ([lb,rt] and [lt,rb], as in Figure 2(a)). Alternative configurations of the capacitor network are also possible, such as vertical ([lb,lt] and [rb,rt], as shown in Figure 2(b)) and horizontal ([lb,rb] and [lt,rt], as in Figure 2(c)). Table 5 lists the sensitivities for selected modes for these alternative configurations. Based on the expressions in Tables 2 and 5, Table 6 lists how specific modes are sensitive or immune to certain types of local manufacturing variations for a particular configuration. Column 1 lists the type of capacitor network configuration. Columns 2 and 3 list the type of variation (odd or even) along the $X$ and $Y$ directions, respectively. The remaining four columns list the sensitivity of four modes to the particular type of variation. Note that '1X' ('1Y') is used to indicate a strong first order dependence on local manufacturing variation along the $X$ ($Y$) axis. Similarly, '1XY' implies dependence on the product of local manufacturing variations along the $X$ and $Y$ axes. Moreover, '0.1' has been used to imply a weak dependence on the corresponding variable while '1' implies a strong dependence. Finally, the entries in Table 6 only indicate a certain level of dependence on local manufacturing variations and not the exact magnitude. Even though Table 6 lists only odd and even type of variations, its scope is general since any function can be expressed[4] as a sum of odd and even functions. Below we give additional details about the more interesting configurations.

1. For horizontal configuration, in the presence of odd variations along both the $X$ and $Y$ axes, mode 0011 is sensitive to variation along the $X$ axis only.

2. For diagonal configuration, in the presence of odd variations along the $X$ axis, mode 0110 is sensitive to variations along the $X$ axis only.

3. For horizontal configuration, in the presence of odd vari-

[4] $f(x) = f_{odd}(x) + f_{even}(x)$, where $f_{odd}(x) = [f(x) - f(-x)]/2$ and $f_{even}(x) = [f(x) + f(-x)]/2$.

| Combdrive configuration | Variation type | | Modes ($lt.rb.lb.rt$) | | | |
|---|---|---|---|---|---|---|
| | $X$ axis | $Y$ axis | 0011 | 0110 | 0101 | 0000 |
| Diagonal | Odd | Odd | 0 | 1X | 1Y | 1XY |
| | Odd | Even | 0.1Y | 1X | 0 | 0 |
| | Even | Odd | 0.1X | 0 | 1Y | 0 |
| | Even | Even | 0.1(X+Y) | 0 | 0 | 0 |
| Horizontal | Odd | Odd | 1X | 0 | 1XY | 1Y |
| | Odd | Even | 1X | 0.1Y | 0 | 0 |
| | Even | Odd | 0 | 0.1X | 0 | 1Y |
| | Even | Even | 0 | 0.1(X+Y) | 0 | 0 |
| Vertical | Odd | Odd | 1Y | 1XY | 0 | 1X |
| | Odd | Even | 0 | 0 | 0.1Y | 1X |
| | Even | Odd | 1Y | 0 | 0.1X | 0 |
| | Even | Even | 0 | 0 | 0.1(X+Y) | 0 |

Table 6: Mode sensitivities under different types of local manufacturing variations and for different sense configurations.

ations along the $Y$ axis, mode 0000 is sensitive to variations along the $Y$ axis only.

4. For diagonal configuration, in the presence of even variations along the $Y$ axis and odd variations along the $X$ axis, mode 0011 is weakly sensitive to variations along the $Y$ axis only.

## 5 Simulation Results

We present simulation results for two different accelerometer sensor designs, whose features are listed in Table 7. Both designs are derived by modifying existing CMOS-MEMS accelerometer designs to include the necessary features required to implement our BIST capability. Specifically, the BIST includes analog multiplexers for switching modulation signals via simple digital control logic [13]. For both designs, the sense combdrives have the diagonal configuration. Simulation experiments are performed to examine the capability of our BIST to detect asymmetry caused by:

1. A single dielectric particle acting as a bridge between a pair of structures where at least one is movable;
2. A variation in vertical misalignment between fixed and movable fingers caused by curl mismatch [25];
3. A variation in local etch [26];
4. Unequal parasitics in the interconnects from the self-test sense points to the differential sense amplifier.

The chosen asymmetries are guided by our interaction with industry as well as our own experience. For example, particles can originate from the clean room but also from the removal of the sacrificial layer during the release step. Particles formed out of the sacrificial layer can be as large as a few $\mu m$ and are therefore large enough to act as bridges between structures.

| Parameter | design 1 | design 2 |
|---|---|---|
| Resonant frequency ($kHz$) | 12.5 | 5.6 |
| Sensor sensitivity ($mV/G$) | 0.88 | 5.2 |
| Modulation voltage amplitude ($V$) | 5 | 3 |
| Actuation voltage amplitude ($V$) | 1.5 | 1.5 |
| Input referred noise ($\mu G/\sqrt{Hz}$) | 100 | 100 |
| Bandwidth of baseband sense signal ($Hz$) | 500 | 500 |
| Nominal value of normal sense mode ($mV$) | 10.5 | 34.4 |
| Resonant frequency range ($kHz$) | 9.4-15.6 | 4.2-7.0 |
| Normal sense output range ($mV$) | 8.4-12.6 | 27.5-41.2 |
| Noise voltage floor ($\mu V$) | 2 | 10 |

Table 7: Nominal values for design and measured parameters of the two accelerometer designs used for simulation.

Simulation experiments were conducted using NODAS [27], a library of mixed-domain, behavioral models written in AHDL (Analog Hardware Descriptive Language) that has been integrated into the flow of a commercial circuit simulation tool. NODAS has been shown to closely match experimental results [26]. The efficacy of NODAS as a reliable and much faster simulator than finite element analysis has also been demonstrated [22]. We simulate both the electromechanical microstructure and electronic circuitry of the accelerometer. The electronic subcircuit is based on a design

| Defect location (%) | Resonant frequency ($kHz$) | Finger sense output for a mode (V) | | Beam sense output for a mode (V) |
|---|---|---|---|---|
| | | **0011** | **0110** | **00** |
| None | 12.53 | 10.52m | -3$\mu$ | -2$\mu$ |
| 10 | 13.12 | 9.58m | -3$\mu$ | -27$\mu$ |
| 20 | 14.00 | 8.40m | -2$\mu$ | -73$\mu$ |
| 30 | 15.32 | 6.98m | -2$\mu$ | -133$\mu$ |

Table 8: Design 1 outputs for a single bridge defect located at different points between spring beam $B_1$ and dummy finger $D_1$ of Figure 1.

| Defect location | Resonant frequency ($kHz$) | Finger sense output for a mode (V) | | | | Beam sense output for a mode (V) |
|---|---|---|---|---|---|---|
| | | **0011** | **0110** | **0101** | **0000** | **00** |
| None | 5.58 | 34.37m | 0 | 0 | 0 | 0 |
| right end of beam $B_2$ and dummy finger $D_4$ | 5.63 | 33.81m | 25$\mu$ | 15p | 5.8n | 384$\mu$ |
| left end of beam $B_4$ and dummy finger $D_8$ | 5.91 | 30.72m | 110$\mu$ | 293p | 23.3n | 482$\mu$ |

Table 9: Design 2 outputs for a single bridge defect located at different points of the spring, between beam $B_2$ ($B_4$) and dummy finger $D_4$ ($D_8$), in the right upper quadrant of Figure 1.

[23] that has been fabricated and validated. A simplified version of the routing of the actuation, modulation, and sense signals is illustrated in Figure 4. The details of the dry etch process, design and representative die-shots are presented in [23]. Self-test by electrostatic actuation of accelerometer sensor is based on the well-known principle that an electrostatic force of attraction is generated between the positive and negative plates of an electric capacitor and is described in [17].

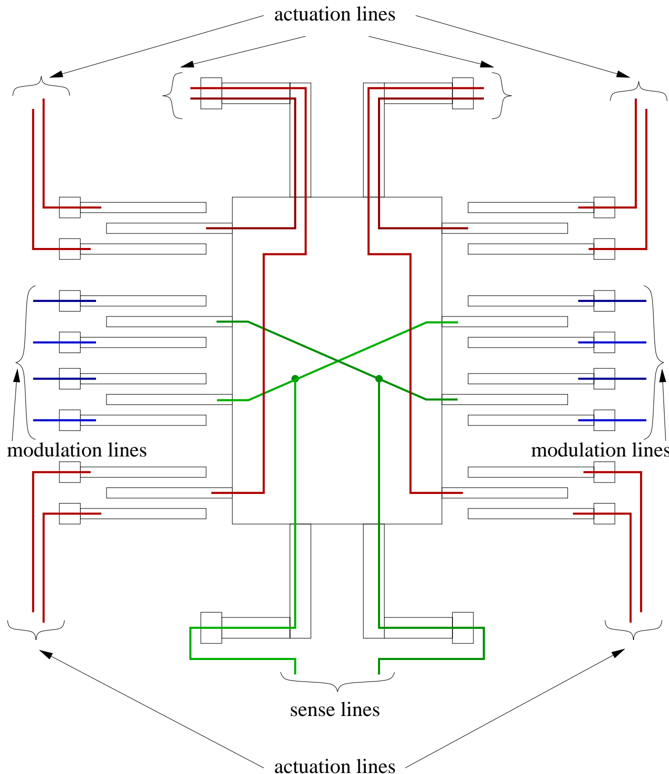

Figure 4: Routing of actuation, modulation, and sense signals through an accelerometer sensor.

One of the parameters used to decide pass/fail for an accelerometer is its resonant frequency for translation in the $Y$ direction (see Figure 1). The acceptable range for resonant frequency includes a maximum deviation of $\pm$25% from the nominal value. Another pass/fail test, called the sensitivity test, uses the normal sense signal (output of mode 0011) which is allowed to deviate at most $\pm$20% from its nominal value. Note that for a given design, any sense signal is considered significant if and only if the signal magnitude exceeds the noise floor for that design. All of these design-specific parameters are listed in Table 7.

In the application of our BIST approach to the accelerometer, self-test outputs are created from normal sense fingers and spring beams [13]. Depending on the particular nature of an asymmetry, one output may be more sensitive than the other at observing the effects of a defect. Also, the asymmetries detected at one output need not be a subset of those detected at the other. Hence, the use of self-test outputs from both beams and fingers, and possibly other sites, may be necessary to minimize defect escapes.

| Defect location (%) | Resonant frequency ($kHz$) | Finger sense output for a mode (V) | | Beam sense output for a mode (V) |
|---|---|---|---|---|
| | | **0011** | **0110** | **00** |
| None | 12.53 | 10.52m | -3$\mu$ | -2$\mu$ |
| 0 | 13.74 | 8.30m | 783$\mu$ | -2$\mu$ |
| 10 | 14.09 | 7.85m | 848$\mu$ | -1$\mu$ |
| 20 | 14.57 | 7.27m | 906$\mu$ | -1$\mu$ |

Table 10: Design 1 outputs for a single bridge defect located at different points between movable finger $M_6$ and fixed finger $S_3$ of Figure 1.

| $\delta H_{right}$ ($\mu m$) | Resonant frequency ($kHz$) | Finger sense output for a mode (V) | | Beam sense output for a mode (V) |
|---|---|---|---|---|
| | | **0011** | **0110** | **00** |
| 0 | 12.53 | 10.52m | -3$\mu$ | -2$\mu$ |
| +0.5 | 12.51 | 10.44m | 55$\mu$ | 5$\mu$ |
| +1.0 | 12.51 | 10.23m | 223$\mu$ | 21$\mu$ |
| +1.5 | 12.51 | 9.87m | 482$\mu$ | 48$\mu$ |
| +2.0 | 12.51 | 9.42m | 806$\mu$ | 80$\mu$ |

Table 11: Design 1 outputs for height mismatch between all fixed and movable fingers on the right side of the sensor.

In the following discussion, for the output from the sense fingers, only four BIST modes (0011, 0110, 0101, and 0000) have been considered for design 2 while a smaller subset (modes 0011 and 0110) have been analyzed for design 1. The sense output from beams [13] involves only two dipoles and can have four possible BIST modes, out of which only two are unique (*e.g.*, 00 and 01). For the purpose of detecting asymmetry, the beam sense mode 00 is sufficient and therefore is the only mode considered. It is also assumed that both the finger sense and beam sense amplifiers are identical.

## 5.1 Beam Bridges

A bridge defect can be caused by particulate matter that attaches a movable beam to an adjacent structure (*e.g*, a dummy finger) thereby hindering its motion. In this analysis the material of the bridging defect is assumed to be dielectric since such defects are harder to detect. Due to the four-fold symmetry of the accelerometer, simulation of a bridge defect has been limited to one quadrant of the layout. Specifically, beam $B_1$ and dummy finger $D_1$ of the upper left quadrant of Figure 1 are used for design 1. Column 1 of Table 8 indicates the defect location expressed as a percentage of beam length. The 0% point is the anchored end of the beam and the 100% point is where the beam meets the shuttle. For design 2, column 1 of Table 9 indicates that the defect is located between beam $B_2$ ($B_4$) and dummy finger $D_4$ ($D_8$) of the upper right quadrant of Figure 1. Columns 2 and 3 list the values of resonant frequency and normal sense output, respectively, for bridge defects located at various locations along the beam(s).

As the defect location moves from the anchor end of the spring to the end where it is attached to the shuttle, the beam stiffness increases. Consequently, shuttle displacement decreases. Also the layout asymmetry becomes more pronounced resulting in an increased output from finger sense mode 0110 (design 2 only) and beam sense mode 00.

The listed resonant frequency values shown in Tables 8-9 are all within the acceptable range, indicating these defects will pass a resonant frequency test. For design 1, the normal sense output is barely outside its acceptable range only for one defect location (at the 30% point). Hence, in a majority of cases, resonant frequency and sensitivity tests will be ineffective. The finger sense mode 0110 is insensitive for design 1 and weakly sensitive for design 2. Other finger sense modes (0101 and 0000 for design 2 only) are insensitive too. This is largely because the stiff shuttle leads to virtually equal displacements on both sides. However, for both designs, the beam self-test mode 00 is very sensitive and strongly indicates

| $\delta H_{right}$ ($\mu m$) | Resonant frequency ($kHz$) | Finger sense output for a mode (V) | | | | Beam sense output for a mode (V) |
|---|---|---|---|---|---|---|
| | | **0011** | **0110** | **0101** | **0000** | **00** |
| 0 | 5.58 | 34.37m | 0 | 0 | 0 | 0 |
| +0.1 | 5.58 | 34.34m | 5.6$\mu$ | 0 | 1.2p | 1.3$\mu$ |
| +0.2 | 5.58 | 34.31m | 22.4$\mu$ | 0 | 4.9p | 2.1$\mu$ |
| +0.5 | 5.59 | 34.15m | 139$\mu$ | 0 | 30p | 7.7$\mu$ |
| +0.7 | 5.59 | 33.93m | 269$\mu$ | 0 | 58p | 14$\mu$ |
| +0.8 | 5.60 | 33.79m | 349$\mu$ | 0 | 75p | 18$\mu$ |
| +1.0 | 5.60 | 33.48m | 537$\mu$ | 1.9p | 115p | 27$\mu$ |

Table 12: Design 2 outputs for height mismatch between all fixed and movable fingers on the right side of the sensor.

| Etch variation ($\mu m$) | Resonant frequency ($kHz$) | Finger sense output for a mode (V) | | Beam sense output for a mode (V) |
|---|---|---|---|---|
| | | **0011** | **0110** | **00** |
| +0.025 | 12.33 | 10.30m | 507$\mu$ | 48$\mu$ |
| +0.020 | 12.37 | 10.34m | 408$\mu$ | 39$\mu$ |
| +0.010 | 12.45 | 10.43m | 205$\mu$ | 19$\mu$ |
| 0 | 12.53 | 10.52m | -3$\mu$ | -2$\mu$ |
| -0.010 | 12.61 | 10.61m | -217$\mu$ | -23$\mu$ |
| -0.020 | 12.69 | 10.71m | -438$\mu$ | -45$\mu$ |
| -0.025 | 12.73 | 10.76m | -551$\mu$ | -56$\mu$ |

Table 13: Design 1 outputs for etch variations between the left and right sides of the sensor.

the presence of an asymmetry.

## 5.2 Finger Bridges

A bridge defect affecting fingers is similar to a beam bridge defect except that it is located between a movable finger and a fixed finger. Naturally, it acts as a hindrance to shuttle motion. Similar to beam bridge defects, the material of the defect is assumed to be dielectric. Like before, the symmetry of the accelerometer is used to limit simulations to the upper right quadrant of the layout. A defect that bridges fingers $M_6$ and $S_3$ in the upper right quadrant of Figure 1 is considered without loss of generality. A finger bridge defect is modeled using the approach described in [22]. Defect location is expressed as a percentage of movable finger length. The 0% point is the movable finger tip, and the 100% point is the movable finger base where it is attached to the shuttle.

The results in Table 10 for design 1 indicate that a finger bridge defect may pass a resonant frequency test but will fail a sensitivity test. However, the normal sense output by itself does not indicate an asymmetry. The beam self-test mode 00 does not detect the finger defect because the defect location is too far from the beams to affect the output of the beam self-test mode. However, the finger self-test mode 0110 clearly indicates the presence of asymmetry.

For design 2, a finger bridge defect causes failure for both resonant frequency and sensitivity tests. Hence, the various BIST modes do not reveal any additional information.

## 5.3 Finger Height Mismatch

Ideally, the fingers should all be at the same height above the die surface. But variations in parameters such as temperature and residual stress can lead to finger height mismatch [25]. Height mismatch between the fixed and movable fingers reduces inter-finger overlap and hence inter-finger capacitance. We show how left-right asymmetry caused by height mismatch can be detected by our BIST approach. Without loss of generality, the finger height mismatch is assumed to exist on the right side of the accelerometer only ($\delta H_{left} = 0$). Tables 11-12 give the simulation results for the two designs. Column 1 lists the relative height mismatch, expressed as $\delta H_{right} - \delta H_{left} = \delta H_{right}$. Results for negative values of mismatch have not been separately simulated since we believe

| Etch variation ($\mu m$) | Resonant frequency ($kHz$) | Finger sense output for a mode (V) | | | | Beam sense output for a mode (V) |
|---|---|---|---|---|---|---|
| | | **0011** | **0110** | **0101** | **0000** | **00** |
| 25 | 5.49 | 33.68m | 1.08m | -5.7p | 179p | 3.7$\mu$ |
| 20 | 5.51 | 33.84m | 0.87m | -3.7p | 143p | 3.1$\mu$ |
| 10 | 5.55 | 34.10m | 0.44m | -0.9p | 74p | 1.9$\mu$ |
| 0 | 5.58 | 34.37m | 0 | 0 | 0 | 0 |
| -10 | 5.60 | 34.68m | -0.46m | 1.0p | -78p | -2.3$\mu$ |
| -20 | 5.63 | 35.02m | -0.93m | 4.1p | -155p | -3.5$\mu$ |
| -25 | 5.65 | 35.18m | -1.17m | 6.5p | -196p | -4.1$\mu$ |

Table 14: Design 2 outputs for etch variations between the left and right sides of the sensor.

| Parasitic mismatch (%) | Resonant frequency ($kHz$) | Finger sense output for a mode (V) | | Beam sense output for a mode (V) |
|---|---|---|---|---|
| | | **0011** | **0110** | **00** |
| 0 | 12.53 | 10.52m | -3$\mu$ | -2$\mu$ |
| 1.25 | 12.51 | 10.50m | -26$\mu$ | -7$\mu$ |
| 2.5 | 12.51 | 10.49m | -49$\mu$ | -11$\mu$ |
| 3.75 | 12.51 | 10.48m | -71$\mu$ | -17$\mu$ |
| 5.0 | 12.51 | 10.47m | -94$\mu$ | -22$\mu$ |

Table 15: Design 1 outputs for variations in the parasitic interconnect capacitance of the differential amplifier.

they would yield similar results. CMOS-MEMS exhibits this nearly symmetric behavior since the gap of $20\mu m$ between the substrate and the sensor fingers is large.

With increasing height mismatch, the difference in capacitance between the left and right increases, as evident from finger sense mode 0110 and beam sense mode 00 (see Tables 11-12). The resonant frequency however remains virtually unchanged. The normal sense output reveals a reduced but acceptable voltage. Hence, tests based on resonant frequency and normal sense output will be ineffective in detecting the asymmetry. However, the output of mode 0110 clearly indicates the presence of asymmetry. Although not as sensitive, the beam self-test mode 00 also varies with the amount of height mismatch and therefore indicates an asymmetry as well.

## 5.4 Local Etch Variation

An etching process is used in fabrication to remove sacrificial material to free the micromechanical sensor. Material removal through an etching process varies with time and space even though such variation is not desirable. For example, a rectangular structure designed to have length $l$ and width $w$ may be subjected to more than the intended etch by a length $\delta$, resulting in dimensions $[l-2\delta, w-2\delta]$. This is due to the fact that each side-wall of the rectangular structure shifts inwards by $\delta$ so that each dimension reduces by $2\delta$. This type of etch variation is called over-etch. In a similar fashion, under-etch causes an oversized structure of size $[l+2\delta, w+2\delta]$.

Etch variation can also be local in nature. Consider two rectangular structures that are designed to be identical but during fabrication they are subjected to different etch variations, $\delta_1$ and $\delta_2$. As a result, the two structures will have different dimensions, causing a mismatch.

Without loss of generality, we assumed in simulation that the accelerometer's left side has nominal etch while the right side has either over- or under-etch. Tables 13-14 give the simulation results for various levels of etch variations. Column 1 lists the etch mismatch between the two sides. The mismatch in etch variation is positive when the right side is more etched than the left side.

As the relative over-etch increases, the capacitance of the right side reduces because of the increase in the inter-finger gap. Consequently, the outputs of finger sense mode 0110 and

| Parasitic mismatch (%) | Resonant frequency ($kHz$) | Finger sense output for a mode (V) | | | | Beam sense output for a mode (V) |
|---|---|---|---|---|---|---|
| | | **0011** | **0110** | **0101** | **0000** | **00** |
| 0 | 5.58 | 34.37m | 0 | 0 | 0 | 0 |
| +2.5 | 5.58 | 34.32m | 3n | 5p | 47.3$\mu$ | 4.3$\mu$ |
| +5.0 | 5.58 | 34.28m | 5n | 10p | 94.5$\mu$ | 7.7$\mu$ |

Table 16: Design 2 outputs for variations in the parasitic interconnect capacitance of the differential amplifier in Figure 3.

beam sense mode 00 increase. For increasing levels of relative under-etch, two counteracting effects become significant. The increased beam thickness on the right side causes increased stiffness which in turn reduces displacement. However, the reduced inter-finger gap causes higher inter-finger capacitance which more than offsets the reduced displacement. In any case, increasing levels of local etch variation lead to greater outputs from finger sense mode 0110 and beam sense mode 00.

Neither a resonant frequency test nor a sensitivity test will detect the presence of this type of asymmetry because both parameters are within their respective tolerance ranges. However, the outputs of finger self-test mode 0110 and beam self-test mode 00 are indicators of asymmetry. As in the case of finger height mismatch, the finger self-test mode 0110 is a stronger indicator of this type of asymmetry as compared to the beam self-test mode 00.

## 5.5 Parasitic Variation

Ideally, the sensing circuitry for self-test should only be sensitive to asymmetries in the micromechanical sensor and not the external electronics (including interconnects). In reality, a difference signal may be due to variation external to the sensor area, such as in the interconnects which carry the self-test sense signals to the inputs of the differential amplifier (see Figure 3). With reference to Figure 3, assume the interconnect capacitances ($C_{p_1}$ and $C_{p_2}$) are unequal. The objective is to determine the extent to which the parasitic capacitance mismatch due to such interconnect asymmetry will produce a significant sense amplifier output. The maximum value of the parasitic mismatch can be used to decide a suitable threshold for detection of sensor asymmetry during self-test. The nominal interconnect capacitance is assumed to be $40fF$. A maximum mismatch of 5% between the two interconnects is considered, assuming that a good layout design and a stable process can restrict such variations to the presumed limit. Without loss of generality, we assumed that $C_{p_1}$ is at its nominal value while $C_{p_2}$ is higher (for both finger and beam outputs). The simulation results are listed in Tables 15-16.

For both designs, the parasitic mismatch has a more pronounced effect on the beam self-test mode 00 as compared to the finger self-test modes since the beam sense signals are much weaker. For design 1, the finger mode 0110 is much less sensitive to variations in the interconnect when compared to local etch variations and finger height mismatch. The same is largely true for the beam self-test mode even though it is more sensitive compared to the finger self-test mode. For design 2, all finger sense modes except 0000 are immune to the parasitic mismatch. The beam self-test mode is marginally sensitive to variations in the interconnect when compared to variations in local etch and finger height.

Interconnect capacitance mismatch does indeed cause self-test outputs to exceed the noise floor in some cases. But, in a majority of the cases considered, the output magnitude does not rival that produced by the other defects. For design 1, only a beam bridge defect that is located close to its anchor point will produce a beam self-test sense signal that is comparable to that produced by interconnect mismatch. In case of design 2, only the finger self-test mode 0000 will produce a weak signal. This implies that variations of up to 5% in the interconnect capacitance are unlikely to falsely indicate asymmetry in the micromechanical structure of the accelerometer.

Even though our simulation has considered the effect

of single defects, two or more of the afore-mentioned defects/perturbations may occur simultaneously [12]. It is not always possible to determine the individual contributions of the perturbations and in many cases it is even difficult to determine all the contributing perturbations themselves. This is largely due to the phenomena of (mis)behavior overlap [12]. The many-to-one nature of the defect-to-(mis)behavior mapping greatly raises the difficulty in the identification of contributing as well as non-contributing perturbations. Moreover, the individual perturbations and their relative contributions are largely dependent on various factors including the manufacturing process and the accelerometer design. In addition, the effective determination of the perturbations and/or their relative contributions is highly dependent on the test/measurement methodology. Therefore, in a limited number of cases, it is possible to predict if a certain misbehavior is very likely due to a particular defect type [30].

# 6 Process Characterization via BIST

In the following, we give examples of how sensitive various modes are to particular instances of local process variations, namely, etch variation. In the following, over-etch and under-etch are arbitrarily assigned positive and negative polarities, respectively.

1. For a diagonal configuration and an odd etch variation along the $X$ axis, the 0011 mode is much less sensitive than the 0110 mode. Simulation results (see rows 1-3 in Table 17) show that the absolute change in voltage output of mode 0110 is about 1.5 times that of mode 0011. In fact, the voltage output of mode 0011 mode changes by only ±2.4% while the voltage output of mode 0110 changes by several orders of magnitude. Incidentally, the sense output for mode 0101 is practically zero as expected (see rows 2-3 in Table 17).

2. For a diagonal configuration, if there are identical odd etch variations along the $X$ and $Y$ axes, modes 0110 and 0101 should produce outputs of the same magnitude. This is confirmed by row 4 in Table 17. As expected, the output for mode 0011 is practically unchanged (see rows 1 and 4 in Table 17).

3. For a diagonal configuration, mode 0000 is expected to give significant output only when there are odd variations along both $X$ and $Y$ axes. This is evident from Table 17 where the output of mode 0000 is negligible in rows 2-3 but significant in row 4.

4. It can be shown that mode 0011 in the vertical configuration is more sensitive to a odd etch variation along the $Y$ axis than mode 0000 in the horizontal configuration. This is confirmed by rows 5-6 of Table 17 which show the output of mode 0011 in the vertical configuration to be about 29% more that the output of mode 0000 in the horizontal configuration.

For every variation type listed in Table 6, it is possible to determine the mode and the network configuration which is most sensitive. Thus, it is possible to select a minimal set of modes (and network configurations) that can capture the same information that all four modes under each of the three network configurations together can capture.

In order to characterize the device, the parameters $\lambda_i$ ($i \in \{lt, rb, lb, rt\}$) need to be computed from measurements from no more than four suitably-chosen BIST modes. Let $T_1$-$T_4$ be the measured sense outputs ($\Delta V_B - \Delta V_A$) for the four modes listed in Table 4 for the diagonal configuration. Using Equation 56, we can compute the values of $\lambda_i$ ($i \in \{lt, rb, lb, rt\}$) as follows:

$$\lambda_{lt} = \frac{C_p}{4C_0}\left[\frac{T_{00} + (T_2 + T_3)}{T_{00} - (T_1 + T_4)} - 1\right] \tag{81}$$

$$\lambda_{rb} = \frac{C_p}{4C_0}\left[\frac{T_{00} - (T_2 + T_3)}{T_{00} - (T_1 + T_4)} - 1\right] \tag{82}$$

$$\lambda_{lb} = \frac{C_p}{4C_0}\left[\frac{T_{00} + (T_2 - T_3)}{T_{00} - (T_1 - T_4)} - 1\right] \tag{83}$$

$$\lambda_{rt} = \frac{C_p}{4C_0}\left[\frac{T_{00} - (T_2 - T_3)}{T_{00} - (T_1 - T_4)} - 1\right] \tag{84}$$

where

$$T_{00} = (V_{mp} - V_{mn})\frac{\delta}{C_0}$$

| Combdrive configuration | Average etch variation in a quadrant ($nm$) | | | | Resonant frequency ($kHz$) | Sense output for a mode $= \Delta V_B - \Delta V_A$ (V) | | | | Calculated local variation parameters (%) | | | |
|---|---|---|---|---|---|---|---|---|---|---|---|---|---|
| | $lt$ | $rb$ | $lb$ | $rt$ | | $T_1$ (**0011**) | $T_2$ (**0110**) | $T_3$ (**0101**) | $T_4$ (**0000**) | $\lambda_{lt}$ | $\lambda_{rb}$ | $\lambda_{lb}$ | $\lambda_{rt}$ |
| Diagonal | 0 | 0 | 0 | 0 | 5.58 | 34.37m ($\pm$ 0%) | 0 | 0 | 0 | 99.98 | 99.98 | 99.98 | 99.98 |
| Diagonal | 0 | +25 | 0 | +25 | 5.49 | 33.68m (-2.0%) | 1.08m | -5.7p | 179p | 99.73 | 93.53 | 99.73 | 93.53 |
| Diagonal | 0 | -25 | 0 | -25 | 5.65 | 35.18m (+2.4%) | -1.17m | 6.5p | -196p | 100.60 | 107.52 | 100.60 | 107.52 |
| Diagonal | 0 | 0 | +25 | -25 | 5.57 | 34.47m (+0.3%) | -1.13m | 1.13m | -46$\mu$ | 100.25 | 100.25 | 94.11 | 107.30 |
| Horizontal | +25 | 0 | 0 | +25 | 5.49 | 0 | 33.70m | 0 | 0.84m | | | | |
| Vertical | +25 | 0 | 0 | +25 | 5.49 | 1.08m | 0 | 33.71m | 0 | | | | |

Table 17: Design 2 test outputs of various BIST modes for various forms of etch variation across the sensor.

In a typical example case, where quadrants *rt* and *rb* are over-etched by $25nm$ (see row 2 in Table 17), we have from NODAS [27] simulation: $V_{mp} = +1.5V$, $V_{mn} = -1.5V$, $T_{00} = 83.39mV$, $\frac{C_p}{4C_0} = 1.426$, $T_1 = 33.68mV$, $T_2 = 1.08mV$, $T_3 \sim T_4 \sim 0$. This gives the calculated values of $\lambda_i$ ($i \in \{lt, rb, lb, rt\}$) in row 2 of Table 17 and these values are expected since the combdrive capacitances on the right half are lower.

Wafer characterization is an extension of device characterization, since collection of data from multiple dice (one die may have one or more devices) will give an estimate of how the $\lambda$ parameter varies across the wafer. Basically, a discrete two-dimensional plot of $\lambda$ over the entire wafer can be used as a measure of manufacturing variations across the wafer.

# 7 Stimuli Generation and Signature Analysis

The actuation voltage amplitude listed in Table 7 refers to the electrostatic actuation-based stimuli used in our simulation experiments. In general, our D-BIST technique is compatible with all industry-standard stimuli generation methods that are also used with other BIST techniques. For example, in case of the accelerometer, both electrostatic actuation and mechanical vibration can be used to generate stimuli for our BIST.

Signature verification for our BIST is achievable in different ways. In case of an accelerometer sensor using diagonal sense configuration, signature verification for the "normal" (0011) mode is no different from current industry-standard BIST techniques which include comparison to a golden reference. However, for the X (0110), Y (0101) and XY (0000) modes, signature verification has a whole new meaning since in a good device, these modes will have practically zero output. Therefore, the issue of signature verification boils down to arbitrarily choosing a threshold for each of these three modes where the choice of such thresholds will depend on process, design, performance and reliability parameters. Without prior knowledge of all of these parameters it is impractical to choose such thresholds since that may lead to false positives and/or false negatives.

# 8 Conclusions

Our differential self-test method described in this work is focused on enhancing observation and therefore complements the existing built-in stimulus generation techniques used in industry and proposed in the literature. We have demonstrated the ability to detect the presence of three defect types that cause local asymmetry which are not detectable by typical specification-based tests that measure either resonant frequency or sensitivity. It has been established, in principle and by simulation, that a test method using pairwise comparison of multiple outputs from corresponding sub-parts of symmetric devices can substantially enhance detection of hard-to-detect defects. While our D-BIST technique can detect some types of misbehavior masking that are not detected by traditional BIST, we do not claim that it is 100% immune to all types of misbehavior masking. In fact, since our method relies on the extraction of signals from device regions of finite and non-zero area, it is clearly based on the *average* behavior exhibited by each of the device regions. By definition, an average

can include contributions that are both less and more than itself which implies that averaging inherently leads to quantities canceling each other partially or totally. Therefore, our method may not detect some types of misbehavior masking where all the contributing perturbations are localized in the same device region (same as "quadrant" in our specific example) from which an output signal is measured.

Our model, when applied to a symmetric microstructure (*e.g.*, the accelerometer sensor), shows that the differential self-test method [13, 14, 15] is a very broad and versatile technique that can also be used for characterization, if appropriate modulation schemes are implemented. Die and wafer characterization can be accomplished if the dependence of sense capacitances on local manufacturing variations is known. The electrical sensitivities measured from the various BIST modes can then be mapped to values of equivalent local manufacturing variations. The current mathematical model also explores a large space and enables customization for characterization of specific types of manufacturing variations. The model is generic and can be easily applied to a device with any number of sub-parts that are identical by design, as described in [15]. The trade-off for our BIST is a marginal increase in design complexity and device area for additional electronics. However, there is no degradation in performance since the additional parasitics introduced by the switching circuitry are adequately driven by the strong modulation signals while the weak sense signals are not over-loaded.

# References


[1] J. A. Walraven, "Introduction to Applications and Industries for Microelectromechanical Systems (MEMS)," *Proc. of International Test Conference*, pp. 674-680, Oct. 2003.

[2] A. Kourepenis, J. Borenstein, J. Connelly, R. Elliott, P. Ward and M. Weinberg, "Performance of MEMS Inertial Sensors," *Position Location and Navigation Symposium*, pp. 1-8, April 1998.

[3] R. Lal, P. R. Apte, N. K. Bhat, G. Bose, S. Chandra and D. K. Sharma, "MEMS: Technology, Design, CAD and Applications," *Proc. of Design Automation Conference*, pp. 24-25, Jan. 2002.

[4] S. Cass, "MEMS in Space," *IEEE Spectrum*, Vol. 38, No. 7, pp. 56-61, July 2001.

[5] T. A. Lober and R. T. Howe, "Surface-micromachining Processes for Electrostatic Microactuator Fabrication," *IEEE Solid-State Sensor and Actuator Workshop, Technical Digest*, pp. 59-62, June 1988.

[6] D. C. Hutchison, K. Ohara and A. Takeda, "Application of Second Generation Advanced Multimedia Display Processor (AMDP2) in a Digital Micro-mirror Array based HDTV," *International Conference on Consumer Electronics (ICCE)*, pp. 294-295, June 2001.

[7] R. S. Payne, S. Sherman, S. Lewis and R. T. Howe, "Surface Micromachining: From Vision to Reality to Vision (accelerometer)," *Proc. of International Solid State Circuits Conference*, pp. 164-165, Feb. 1995.

[8] R. Oboe, "Use of MEMS based Accelerometers in Hard Disk Drives," *Proc. of International Conference on Advanced Intelligent Mechatronics*, Vol. 2, pp. 1142 -1147, 2001.

[9] T. Jiang and R. D. Blanton, "Particulate Failures for Surface-Micromachined MEMS," *Proc. of International Test Conference*, pp. 329-337, Sept. 1999.

[10] A. Hartzell and D. Woodilla, "Reliability Methodology for Prediction of Micromachined Accelerometer Stiction," *Proc. of Reliability Physics Symposium*, pp. 202-205, March 1999.

[11] A. Kolpekwar, R. D. Blanton and D. Woodilla, "Failure Modes for Stiction in Surface-Micromachined MEMS," *Proc. of International Test Conference*, pp. 551-556, Oct. 1998.

[12] N. Deb and R. D. Blanton, "Analysis of Failure Sources in Surface-Micromachined MEMS," *Proc. of International Test Conference*, pp. 739-749, Oct. 2000.

[13] N. Deb and R. D. Blanton, "Built-In Self-Test of CMOS-MEMS Accelerometers," *Proc. of International Test Conference*, pp. 1075-1084, Oct. 2002.

[14] N. Deb and R. D. Blanton, "Multi-Modal Built-In Self-Test for Symmetric Microsystems," *Proc. of VLSI Test Symposium*, pp. 139-147, April 2004.

[15] N. Deb and R. D. Blanton, *U. S. Patent Pending, Application No. 10/666,147*, Filed Sept. 18, 2002.

[16] D. De Bruyker, A. Cozma and R. Puers, "A Combined Piezoresistive/Capacitive Pressure Sensor with Self-test Function based on Thermal Actuation," *Proc. of Solid State Sensors and Actuators*, Vol. 2, pp. 1461-1464, 1997.

[17] H.V. Allen, S.C. Terry and D.W. de Bruin, "Self-Testable Accelerometer Systems," *Proc. of Micro Electro Mechanical Systems*, pp. 113-115, 1989.

[18] B. Charlot, S. Mir, F. Parrain and B. Courtois, "Electrically Induced Stimuli for MEMS Self-Test," *Proc. of VLSI Test Symposium*, pp. 210-215, Apr.-May 2001.

[19] R. Rosing, A. Lechner, A. Richardson and A. Dorey, "Fault Simulation and Modelling of Microelectromechanical Systems," *Computing and Control Engineering Journal*, Vol. 11, No. 5, pp. 242-250, Oct. 2000.

[20] W. C. Tang, T.-C. H. Nguyen, M. W. Judy and R. T. Howe, "Electrostatic Comb Drive of Lateral Polysilicon Resonators," *Sensors and Actuators A*, Vol. 21, Nos. 1-3, pp. 328-331, Feb. 1990.

[21] J. Xuesong, J. I. Seeger, M. Kraft and B. E. Boser, "A Monolithic Surface Micromachined Z-axis Gyroscope with Digital Output," *Symposium on VLSI Circuits*, pp. 16-19, 2000.

[22] N. Deb and R. D. Blanton, "High-Level Fault Modeling in Surface-Micromachined MEMS," *Proc. of Design, Test, Integration and Packaging of MEMS/MOEMS*, pp. 228-235, May 2000.

[23] J. Wu, G. K. Fedder and L. R. Carley, "A Low-Noise Low-Offset Chopper-Stabilized Capacitive-readout Amplifier for CMOS MEMS Accelerometers," *Proc. of International Solid State Circuits Conference*, pp. 428-429, Feb. 2002.

[24] H. Luo, G. K. Fedder and L. R. Carley, "A 1 mG Lateral CMOS-MEMS Accelerometer," *Proc. of Micro Electro Mechanical Systems*, pp. 502-507, Jan. 2000.

[25] H. Lakdawala and G. K. Fedder, "Temperature Stabilization of CMOS Capacitive Accelerometers," *Journal Of Micromechanics And Microengineering*, Vol. 14, No. 4, pp. 559-566, April 2004.

[26] Q. Jing, H. Luo, T. Mukherjee, L. R. Carley and G. K. Fedder, "CMOS Micromechanical Bandpass Filter Design Using a Hierarchical MEMS Circuit Library," *Proc. of Micro Electro Mechanical Systems Conference*, pp. 187-192, Jan. 2000.

[27] Q. Jing, T. Mukherjee and G. K. Fedder, "Schematic-Based Lumped Parameterized Behavioral Modeling for Suspended MEMS," *Proc. of International Conference on Computer Aided Design*, pp. 367-373, Nov. 2002.

[28] D. A. Koester, R. Mahadevan and K. W. Markus, *MUMPS Introduction and Design Rules*, MCNC MEMS Technology Applications Center, 3021 Cornwallis Road, Research Triangle Park, NC, Oct. 1994.

[29] R. Difrenza, P. Llinares, S. Taupin, R. Palla, C. Garnier and G. Ghibaudo, "Comparison Between Matching Parameters and Fluctuations at the Wafer Level," *Proc. of International Conference on Microelectronic Test Structures*, pp. 241-246, April 2002.

[30] N .Deb, *Defect Oriented Test of Inertial Microsystems*, Ph.D. thesis, Carnegie Mellon University, Pittsburgh, Oct. 2004.